Quantum defects from a single surface exhibit strong mutual interactions

Chih-Chiao Hung,[1,2,3,*] Tim Kohler,[1] and Kevin D. Osborn[1,2,4,†]

[1] *Laboratory for Physical Sciences, 8050 Greenmead Drive, College Park, Maryland 20740, USA*
[2] *Quantum Materials Center, University of Maryland, College Park, Maryland 20742, USA*
[3] *Department of Physics, University of Maryland, College Park, Maryland 20742, USA*
[4] *Joint Quantum Institute, University of Maryland, College Park, Maryland 20742, USA*

(Received 12 February 2023; revised 11 December 2023; accepted 20 March 2024; published 10 April 2024)

Two-level system (TLS) defects constitute a major decoherence source of quantum information science, but they are generally less understood at material interfaces than in deposited films. Here we study surface TLSs at the metal-air interface, by probing them using a quasiuniform field within vacuum-gap (VG) capacitors of resonators. The VG capacitor has a nanogap that creates an order-of-magnitude larger contribution from the metal-air interface than typical resonators used in circuit QED. We measure three phenomena and find qualitative agreement with an interacting TLS model, where near-resonant TLSs experience substantial frequency jitter from the state switching of far-detuned low-frequency TLSs. First, we find that the loss in all of our VG resonators is weakly or logarithmically power dependent, in contrast to data from deposited dielectric films. Second, we add a saturation tone with power $P_{\rm in}$ to a transmission measurement and obtain the TLS Rabi frequency Ω_0. These data show a substantially weaker $P_{\rm in}$ dependence of Ω_0 than the prediction from the standard noninteracting TLS model. Lastly, we increase the temperature and find an increased TLS jitter rate and dephasing rate from power-dependent loss and phase noise measurements, respectively. We also anneal samples, which lowers the low-frequency TLS density and jitter rate, but the single-photon loss is found to be unchanged. The results are qualitatively consistent with a fast-switching interacting TLS model and they contrast the standard model of TLSs that describes TLSs independently.

DOI: 10.1103/PhysRevApplied.21.044021

I. INTRODUCTION

Suppressing dissipation and noise by choosing materials with a low defect density is essential for superconducting [1,2] and semiconducting [3] qubits. These defects are known as two-level systems (TLSs) due to their characteristic two energy levels [4,5] and cause energy absorption through their dipole moment p. For instance, SiN_x and SiO_2 host TLSs at a known density, which limits the coherence time of qubits [1,6]; presently most qubits do not use these dielectrics but still rely on the AlOx dielectric in the Josephson-junction (JJ) barrier. Additionally, kinetic-inductance photon detectors [7,8], quantum-limited microwave amplifiers [9], and quantum transducers [10,11] can be affected by TLSs. TLSs are located in all known deposited dielectric films [1,6], and material interfaces including surface oxides [12–15]. There are attempts to prevent the growth of the native oxide of metals using vacuum packaging [16] or to reduce it by hydrogen fluoride treatment [15,17]. Understanding and mitigating TLSs can further improve the quality of low-temperature devices.

Measuring the loss $1/Q_i$ (the inverse of the quality factor) of a resonator as a function of the photon number $n_{\rm ph}$ provides a standard way to extract information on TLSs [4,5]. A standard fitting formula for this purpose is

$$\frac{1}{Q_i} = \frac{1}{Q_i^0}\frac{\tanh(\hbar\omega_c/2k_BT)}{(1+n_{\rm ph}/n_c)^{\phi}}, \tag{1}$$

which depends on a loss constant $1/Q_i^0$, resonator frequency ω_c, temperature T, and the crossover photon number $n_c = n_c(\mathbf{p}_i, \mathbf{E}_{\rm zp}(\mathbf{r}), \tau_i)$, where the latter depends on TLS dipole moments $\mathbf{p}_i$, the zero-point electric field $\mathbf{E}_{\rm zp}$, and the TLS coherence time τ_i. Recent measurements of resonators with deposited films support the saturation power law with an exponent of $\phi = 0.5$ [1,18–21]. However, planar resonators with oxide interfaces and possibly also processing residues have a saturation exponent $\ll 0.5$ [22–26].

Generally, there are different possible causes for the weak power dependence ($\phi \ll 0.5$). One possibility is that this is caused by strong TLS-TLS interactions that lead to fast TLS frequency switching. Instead, there may be

*Corresponding authors. chih-chiao.hung@riken.jp
†osborn@lps.umd.edu

wide distributions in p [24,27], $\mathbf{E}_{zp}(\mathbf{r})$ [12,22,28], or τ [29]. Dielectric films sometimes exhibit a large distribution width in p [27,30,31] and planar resonators have a position-dependent field distribution of $\mathbf{E}_{zp}(\mathbf{r})$ [12], which results in an effective distribution of n_c.

Recent experiments show substantial interactions in qubits, including strong TLS spectral diffusion and telegraphic noise [32], and avoided crossings [33]. These are beyond the standard tunneling model (STM) of TLSs, which should describe deposited films, and relates to early work in TLS-TLS interactions [34,35]. In the recent theory of Ref. [36], the authors derived a fast jitter rate γ. Their model describes how the energy of coherent TLSs (CTLSs; in the regime of $\hbar\omega \gg k_B T$) depend on the states of neighboring low-frequency (LF) TLSs (with $\hbar\omega \leq k_B T$). The model uses LF TLSs with a $1/f$ spectral density to create the known $1/f$ noise spectrum of the CTLSs. As a result of the frequency jitter, the power dependence for TLS saturation is weaker than in the STM. The stochastic fluctuations yield a logarithmic equation that appears phenomenologically as a low ϕ [25,26]. However, this data set was taken using planar resonators, where the above concerns from field and TLS distributions are difficult to distinguish (and separately analyze). For scientific understanding, it is important to verify the correct explanation by some means.

Novel experimental techniques have recently been developed to further understand TLSs. An experiment that injected a detuned pump tone to a resonator revealed the average TLS decoherence rate Γ_2 and the TLS coupling rate g [37] (or Rabi frequency Ω [38]). Applying static strain [39], a dc electric field [27,30], or an ac low-frequency electric field [31,40,41] allows the extraction of p-distribution information. Besides the conventional view of defects as atomic systems [4,5], an experiment of NbN resonators shows that trapped quasiparticles might be another possible origin of surface TLSs [42].

Many studies of TLSs explore thermally grown aluminum oxide AlO_x, which is used in most JJs and appears on the surface of Al. The loss tangent of AlO_x is found to be about 2×10^{-3} in large JJs and bulk dielectric [1,43]. Recently, a qubit with a large JJ as a shunt capacitor suggests that transmons are not limited by junction loss. [44]. One set of transmon qubit studies finds that 40% of the individual TLSs are located in the JJ barrier and the rest are on surfaces [45,46]. In another study, the Al metal-air interface with its oxide is found to be the dominant loss mechanism in a qubit type [47]. There are very few studies of TLSs at the surface-air interface.

Here we use vacuum-gap (VG) capacitors in resonators, where the metal-air (MA) interfaces (i.e., AlO_x) within them are the dominant TLS-host materials. Additionally, we fabricate the VG capacitors with a nearly uniform plate gap such that we probe with a nearly uniform ac electric field. Our MA filling factor F_{MA} is as large as 0.9%, assuming a 2-nm surface dielectric thickness and a dielectric constant of 10. This filling factor is 10 times larger than in a typical planar resonator design [14]. Our data show a weak n_{ph}-dependent loss and a weak n_{ph}-dependent Rabi frequency from a pumping tone, which allows us to rule out the possibility of multiple contributions, e.g., p, to these low slopes. The power spectral density of the resonator transmission rate S_{21} at various temperatures indicates that the temperature-dependent TLS dephasing rate is affected by LF TLSs. Lastly, the jitter rate γ decreases after annealing the devices in vacuum at 300 °C, but Q_i^0 is unchanged, indicating that the LF TLS density decreases, but not the near-resonant TLS density. The design of resonators also allows us to apply a dc electric field on the capacitors for the tuning of TLS energies. From the data, we extract $p = 1.5^{+0.8}_{-0.6}$ D and g of the order of 100 kHz. However, individual TLSs are not observed during dc electric field biasing because of the large TLS jitter rate.

II. THEORETICAL MODELS OF TLS LOSS

According to the STM [4,5], under the condition of a uniform ac electric field E_0 and a single-value dipole moment p_c, the loss tangent from TLSs can be written as

$$\tan\delta_{TLS} = \frac{\pi P_0 p_c^2}{3\varepsilon\sqrt{1 + E_0^2/E_c^2}}, \tag{2}$$

where P_0 is the TLS spectral density, ε is the dielectric constant, and the critical field $E_c \propto 1/(p_c\tau)$. LC resonators with parallel-plate capacitors are useful to study the loss tangent of dielectric films since there is only one dominant TLS host volume V, giving $E_0 = \sqrt{2n_{ph}\hbar\omega_c/\varepsilon V}$.

On the other hand, in a planar resonator design, E_0 is nonuniform and the dominant interface contributing to material interface loss is often unknown [47]. An integral over all contributions is necessary, leading to

$$\frac{1}{Q_i} = \frac{\int_V \varepsilon(\mathbf{r})|E_0(\mathbf{r})|^2 \tan\delta_{TLS}(\mathbf{r})\, d\mathbf{r}^3}{\int_V \varepsilon(\mathbf{r})|E_0(\mathbf{r})|^2\, d\mathbf{r}^3}, \tag{3}$$

where $\mathbf{r}$ is the position [12,22,28], and the spatial dependence to the field $E_0(\mathbf{r}) = 2E_{zp}(\mathbf{r})\sqrt{n_{ph}}$ is related to the zero-point fluctuation field E_{zp}. In a constituent volume V_i (add integral sub-$V_i d^3r$ formula), the TLS properties (P_0, p, $\mathbf{E}_{zp}$, and τ) are assumed to be the same and we define the filling factor $F_i = \int_{V_i} \varepsilon(\mathbf{r})|E_0(\mathbf{r})|^2\, d\mathbf{r}^3 / \int_V \varepsilon(\mathbf{r})|E_0(\mathbf{r})|^2\, d\mathbf{r}^3$. Therefore, an approximate expression for analyzing different material volumes hosting TLSs is [24]

$$\frac{1}{Q_i} = \sum_i F_i \tan\delta_{TLS,i} = \frac{1}{Q_i^0(1 + n_{ph}/n_c)^\phi}. \tag{4}$$

After fitting many resonators to this formula, it is unclear if small ϕ is caused by a distribution in $\mathbf{E}_{zp}$ resulting from the resonator geometry, or a wide distribution in TLS parameters p and τ, or large intrinsic TLS jitter. The summation in the previous formula represents TLS populations with different contributions, and thus it may describe a multicontribution (MC) model (see also the fits of Q_i in Appendix A). When the jitter rate γ of TLSs is larger than Ω, the STM is no longer valid [26,36,48]. Instead, theory gives a logarithmic function for the loss tangent

$$\tan\delta_{\mathrm{TLS}} = P_\gamma \tan\delta^0 \tanh\left(\frac{\hbar\omega_c}{2k_BT}\right)\ln\left(\frac{\gamma_{\max}}{\Omega}+C_1\right). \quad (5)$$

Here, $\tan\delta^0$ is the intrinsic loss and $P_\gamma = \ln^{-1}(\gamma_{\min}/\gamma_{\max})$, where $\gamma_{\max}$ and $\gamma_{\min}$ are the maximum and minimum jitter rates of LF TLSs in the model (respectively), and C_1 accounts for the n_{ph}-independent loss. Equation (5) describes a fast-switching (FS) model for unstable CTLS frequencies, and contrasts the MC model that is built upon the STM.

The fits of MC and FS models, Eqs. (4) and (5), respectively, can be distinguished in this work. Although Eq. (5) fits well in Refs. [25,26], the authors are not able to isolate or distinguish loss from multiple interfaces, such that the MC interpretation may be correct. In this article, we probe resonators with a nanogap VG capacitor, limited by TLSs in the surface oxide of Al, and we find that the FS model is appropriate to explain our various data types (including loss).

III. FABRICATION METHOD

The schematic of the resonators follows Refs. [27,30] and is shown in Fig. 1(a). VG-based elements can provide a small on-chip footprint of capacitance and still maintain high quality for both micro- and mechanical wave resonators [49–51]. Vacuum-gap capacitors (VGCs) are achieved with a standard optical lithography process; two kinds of sacrificial layers (SLs) are used, which are low-stress SiN_x and photoresist (PR). The capacitors comprise perpendicular strips of widths 6 and 13 μm. After releasing the SL, the top electrode strip shape ensures a quasiuniform gap distance. At the start of the fabrication, the bottom electrode and the ground plane are made from 120-nm-thick aluminum film deposited by *e*-beam evaporation to ensure a low-stress film. Next, we deposit the SL and name the resonators the SiN_x VGC and PR VGC, depending on the use of the SL. For SiN_x VGCs, we grow 200-nm-thick SiN_x in an Oxford PECVD system at 300 °C and spin PR to pattern the vias and bridge supports. Later, we etch the patterns by SF_6 reactive-ion etching (RIE) plasma. For PR VGCs, we spin S1805 positive PR at 500 nm thickness, and then expose the pattern for vias and bridges. Finally, we developed it with Microposit MF-CD-26. We reduce the PR thickness from 500 to 200 nm by a timed RIE oxygen plasma descum and then bake it at 170 °C to strengthen the PR. A top Al layer of 300 nm is deposited by *e*-beam evaporation and patterned to form the top electrode plate. We choose 300-nm-thick Al in order to fill vias and strengthen the base piles for the top electrodes. Side-view illustrations of two VGCs are shown in Fig. 1(b). An additional thinning process is made by etching 100–200 nm of the top electrode to prevent the bridge from collapsing. The thinning process reduces the beam mass/thickness that changes the strain from compressive to tensile. We show a SiN_x VGC without the thinning process in Fig. 1(c) and a PR VGC with 200 nm thinning in Fig. 1(d). The thinning process is essential for PR VGCs generally and both types of VGC if the support piles have large separations. The separation of piles is chosen as 9 μm in the final devices, and a separation > 15 μm always collapsed after releasing.

Next, the wafers are diced into 6.5×6.5 mm^2 chips and the SL is ready to be released. For the PR VGC, the chips

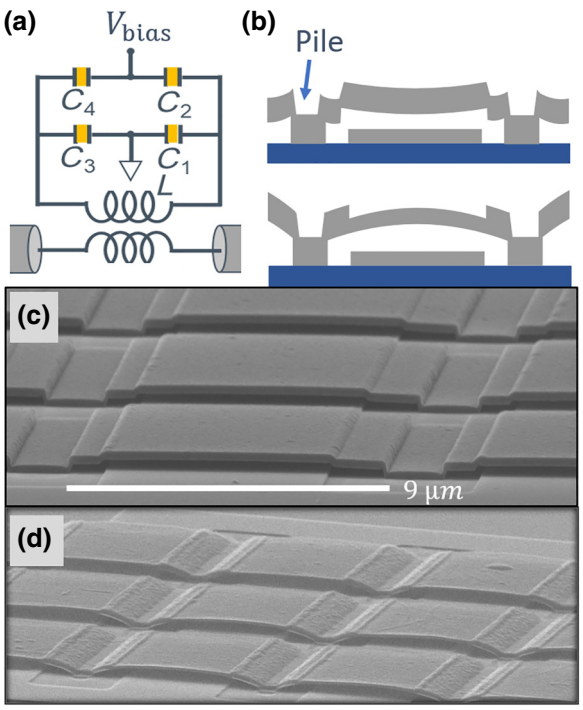

FIG. 1. Schematic, side views, and scanning electron micrographs of vacuum-gap capacitors (VGCs). (a) Schematic of the resonators. (b) Side-view illustrations of the VGCs using SiN_x (top) and photoresist (bottom) as sacrificial layers (SLs). The shape of the top electrode depends on the SLs (see the main text). (c) VGCs with SiN_x as the SL, which yields a terraced bridge shape with an approximate average gap distance $\bar{d} \approx 125$ nm. (d) VGCs with photoresist as the sacrificial layer, which yields an arch shape and $\bar{d} \approx 250$ nm. The process uses a 200-nm metal-thinning step before the removal of the SL. Both types of VGCs have variation in d of less than 15%.

are immersed in 80 °C *n*-methylpryolidone for 3 h, rinsed with isopropyl alcohol, and blown dry by nitrogen. For the SiN_x VGC, the chips are placed under a high power inductively coupled SF_6 plasma without forward voltage, which has a lateral etch rate of around 4 μm per hour. Finally, we measure the resistivity from the bias port of the resonators and the ground to confirm a noncollapsed VGC, where the yield is more than 95%. The gap distance d depends on the choice of the SL and the thinning process. We expect the curvature or d would change during cooling from room temperature to millidegrees kelvin. However, this effect would be small and in fact all noncollapsed VGCs did survive cooling to cryogenic temperatures.

The gap d is estimated by comparing the measured resonant frequency to that of the finite-element microwave simulation in COMSOL Multiphysics®. We find that the d of all four resonators on the same chip have the same value. However, because of the strain, the top electrode bridges are never precisely parallel to the bottom electrodes [see Fig. 1(b)]. By assuming that d is a quadratic equation, we find that the coefficient of variation of d is $< 15\%$ for both types of VGC. From the simulation, we found that the average gap distance $\bar{d}$ from SiN_x VGCs is 125 nm for the no thinning process [Fig. 1(c)], 135 nm for a 100-nm thinning process, and 150 nm for a 200-nm thinning process. The F_{MA} are (0.9%, 0.8%, 0.7%), respectively, and F_r of other interfaces is an order of magnitude lower than that in Ref. [14]. While PR VGCs in Fig. 1(d) have $\bar{d} = 225$ nm and $F_{MA} < 0.45\%$, which is smaller than our other resonators, it should have more contributions to interfaces other than MA relative to SiN_x VGCs. Since the MA surface loss dominates, the surface loss tangent is $\tan\delta_{MA} = (Q_i F_{MA})^{-1}$.

IV. TLS LOSS AND NOISE DATA

The microwave setup is given in Ref. [27], and has a strongly attenuated input line and a low-pass filtered bias line. Six chips are measured, consisting of four SiN_x VGCs and two PR VGCs, and each chip contains four resonators. All resonators worked with repeatable resonant frequencies between cooldowns, except one that may have a collapsed capacitor. An internal quality factor in the single-photon regime $Q_i^0 \gtrapprox 60 \times 10^3$ is found in SiN_x VGCs, regardless of the thinning process. The internal quality factor $Q_i^0 \gtrapprox 20 \times 10^3$ found in PR VGCs is possibly lower due to the ICP dry-etching thinning process causing extra residues. A control group of coplanar waveguide resonators fabricated along with the VGC fabrication process shows a high internal quality factor, $Q_i^0 > 0.5 \times 10^6$, independent of the choice of SL (SiN_x or PR), as expected. The SiN_x VGCs have an MA surface loss tangent of $\tan\delta_{MA} = 1.9 \times 10^{-3}$, assuming the standard native oxide thickness of Al (2 nm, as mentioned above). This is a loss tangent that is comparable to previous large-area loss measurements of AlOx mentioned above, and in a recent study of thin deposited films by the authors [27]. Thus we deem that the MA interface in SiN_x VGCs is dominated by AlOx loss, and we focus on this VGC type in the analysis below.

Because of the unstable TLS frequencies, Q_i fluctuates over time. Therefore, each $Q_i(n_{ph})$ in Fig. 2 is an average value from ten acquisitions of transmission S_{21} and the separation time of two acquisitions approximates 1.5 h. Weak n_{ph}-dependent losses of a SiN_x VGC (black) and a PR VGC (green) are found in all VGCs, where ϕ is 0.18–0.22. Their traces fit well to the logarithmic Eq. (5) derived from the FS model, as shown by the red dashed line. The $Q_i(n_{ph})$ of VGCs follows Eq. (5) up to a certain n_{ph}, but starts to increases afterward (see Appendix C). We only analyze data that is an order of magnitude smaller in the photon number than where the loss reverses. From the fit, we obtain $\gamma_{max} = 2\pi \cdot 5.7$ MHz and $\gamma_{min} = 2\pi \cdot 20$ kHz using $p = 1.5$ (D), which is extracted later in Fig. 2(d). We obtain $F_{MA} P_r \tan\delta^0 \ln(C_1) < 4 \times 10^{-7}$, indicating that the n_{ph}-independent loss is trivial and not affected by the accuracy of the fitting. In contrast, for the deposited AlO_x (obtained from our resonator with a capacitor filled with AlOx), we find a good fit to Eq. (4) with $\phi = 0.5$, as shown by the blue dots in Fig. 2(a). This deposited-film AlO_x data came from a device used in a previous study, where we found some spectral diffusion and jitter from individual TLSs [27]. However, since the power saturation of loss is strong and agrees with the STM, it implies small mutual interactions between CTLSs and the LF TLSs, from the analysis of this measurement. The larger γ in MA TLSs compared to deposited-film TLSs is possibly due to a larger LF TLS density in its AlO_x.

To further understand these MA TLSs, we perform two-tone spectroscopy, where the energy of the first tone is a weak probe (about $0.1\hbar\omega_c$) and the second tone saturates TLSs at frequency ω_{pu} [37,38]. For a saturation tone detuned by $\Delta\omega_{pu} = \omega_{pu} - \omega_c > 0$ from the original resonator frequency ω_c, both the resulting resonance ω_c' and internal quality factor Q_i' would increase because of the reduced TLS ground-state population on the upper side of ω_c. The complex frequency shift created by a single TLS is

$$\delta\omega + i\left(\frac{\delta\Gamma_i}{2}\right) = \frac{g^2}{(\omega_{TLS} - \omega_c) + i\Gamma_2}\sigma_{z0}(\omega_{TLS}, \omega_{pu}, \Omega), \tag{6}$$

where the ground-state population σ_{z0} is a function of the TLS frequency ω_{TLS}, ω_{pu}, and Ω [37]. The real and imaginary parts of Eq. (6) determine the shift in resonance $\delta\omega$ and internal decay rate $\delta\Gamma_i$, respectively, and the collective effect requires a summation over all TLSs. The resulting frequency shift $\Delta\omega = \sum_{TLS}\delta\omega = \omega_c' - \omega_c$ and

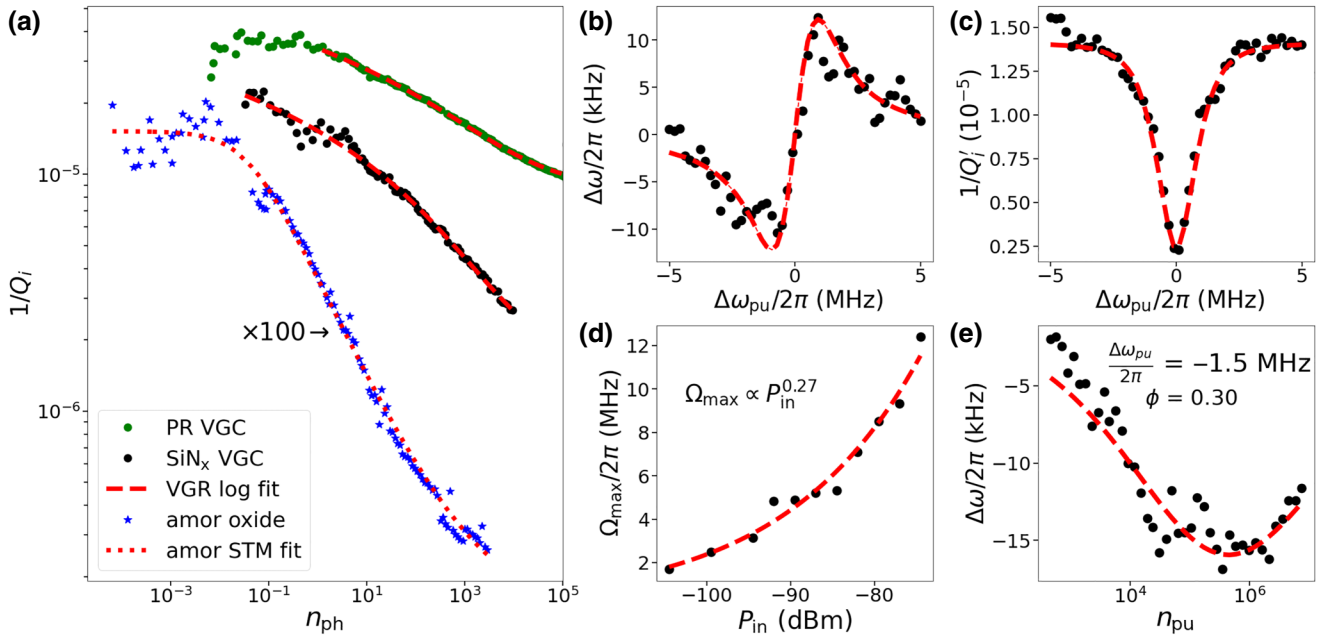

FIG. 2. (a) Intrinsic loss Q_i^{-1} versus the average photon number $n_{\rm ph}$. The resonator results of a photoresist (PR) VGC, a SiN_x VGC, and a bulk amorphous AlO_x sample are displayed from top to bottom, where the AlO_x loss is taken from Ref. [27] and is offset on the logarithmic scale such that multiplication by 100 restores the true values. For the amorphous sample (blue), the single-photon loss is 1.5×10^{-3} and the saturation slope follows the standard TLS model (STM), where the fit to Eq. (2) (shown) has the expected exponent of $\phi = 0.50$. However, the VGC results fit to the FS model [Eq. (5)], which is a logarithmic function, and we have no need for an MC interpretation (see Appendix A for a valid regime). (b)–(e) Two-tone spectroscopy with a pumping tone frequency $\omega_{\rm pu}$, probed around the original resonant frequency ω_c. (b) Resonant frequency shift $\Delta\omega = \omega_c' - \omega_c$ versus the pumping tone detuning $\Delta\omega_{\rm pu} = \omega_{\rm pu} - \omega_c$. (c) Intrinsic loss Q_i^{-1} versus $\Delta\omega_{\rm pu}$. Panels (b) and (c) show the two-tone data from the SiN_x VGC at a fixed input power $P_{\rm in} \approx -105.5$ dBm. The red curves are the simultaneous least-squares fit of both $\Delta\omega$ and Q_i to Eqs. (7) and (8) except for a replacement of $n_{\rm pu}^{0.5} \to n_{\rm pu}^{\phi}$, where ϕ allows a deviation from the STM. From the fit, we obtain the maximum Rabi frequency of TLSs $\Omega_{\rm max} = 2\pi \cdot 1.7$ MHz. (d) Plot of $\Omega_{\rm max}$ versus $P_{\rm in}$, with the fit line $\Omega_{\rm max} \propto P_{\rm in}^{0.27}$. Since the exponent is < 0.5 and shows a weak input power dependence, the data are consistent with the FS model. (e) Plot of $\Delta\omega$ versus $n_{\rm pu}$ for a fixed $\Delta\omega_{\rm pu} = -2\pi \cdot 1.5$ MHz [Eqs. (7)–(9)]. The fit yields $\phi = 0.30$, which is consistent with the weak dependence described by the FS model.

quality factor Q_i' [38] are written as

$$\frac{\Delta\omega}{\omega_c} = \frac{3\pi}{4\sqrt{2}Q_i^0} X_\Delta \frac{\sqrt{1+X_\Delta^2}-1}{\sqrt{1+X_\Delta^2}+1} \tag{7}$$

and

$$\frac{Q_i^0}{Q_i'} = 3X_\Delta^2\left[2+\sqrt{1+2X_\Delta^2}\ln\left(1+X_\Delta^{-2}-\sqrt{1+2X_\Delta^{-2}}\right)\right]. \tag{8}$$

The dimensionless pump frequency $X_\Delta = \Delta\omega_{\rm pu}/\Omega_0$ is dependent on the TLS Rabi frequency Ω_0, which in turn is a function of the photon number $n_{\rm pu}$ in the cavity,

$$\hbar\Omega_0 = 2\langle|\mathbf{p}\cdot\mathbf{E}_{\rm zp}|\rangle\sqrt{n_{\rm pu}}, \tag{9}$$

where the angle brackets $\langle\cdot\rangle$ denote an expectation value. The photon number resulting from the pump tone $n_{\rm pu}$ can be obtained from the pumping power $P_{\rm in}$ by

$$n_{\rm pu} = \frac{2\kappa}{4\Delta\omega_{\rm pu}^2 + \kappa_{\rm tot}^2}\frac{P_{\rm in}}{\hbar\omega_{\rm pu}}, \tag{10}$$

where $\kappa_{\rm tot}$ and $\kappa = 2\pi \cdot 200$ kHz are the total and external decay rates of the resonator, respectively. Typically, in planar resonator designs, the position dependence of $\mathbf{E}_{\rm zp}$ obscures the extraction of p from Ω_0. However, in our VGC most of the energy ($> 85\%$) is in the gap such that $\mathbf{E}_{\rm zp} \approx \sqrt{\hbar\omega_c/2Cd^2}\hat{z}$ [52], where $\hat{z}$ is the normal direction to the plate. Therefore, p can be obtained from the two-tone technique.

From our results of the two-tone spectroscopy, we realize that a similar phenomenological exponent ϕ is needed to fit the data ($n_{\rm pu}^{0.5} \to n_{\rm pu}^{\phi}$) and that

$$\hbar\Omega_0 = 2\langle|\mathbf{p}\cdot\hat{z}|\rangle|\mathbf{E}_{\rm zp}|\, n_{\rm pu}^{\phi}. \tag{11}$$

First, we show $\Delta\omega$ versus $\Delta\omega_{\rm pu}$ [Fig. 2(b)] and $1/Q_i'$ versus $\Delta\omega_{\rm pu}$ [Fig. 2(c)] at a fixed $P_{\rm in} \approx -105.5$ dBm. The red

curves are the simultaneous least-squares fit of both $\Delta\omega$ and Q_i' to Eqs. (7) and (8). From the fit, we obtain $\phi = 0.3$ and $\Omega_{\max} = \Omega_0(\Delta\omega_{\rm pu} = 0) = 2\pi \cdot 1.7$ MHz, which is also the maximum of the Rabi frequency at $\Delta\omega_{\rm pu} = 0$ and at a fixed $P_{\rm in}$. We plot $\Omega_{\max}$ versus $P_{\rm in}$ in Fig. 2(d), which leads to $\phi = 0.27$ and is consistent with an FS model ($\phi < 0.5$). Similarly, we measure the $1/Q_i'$ and $\Delta\omega$ versus $n_{\rm pu}$ at a fixed $\Delta\omega_{\rm pu} = 2\pi \cdot 1.5$ MHz, and the fit yields $\phi = 0.3$ in Fig. 2(e). It is worth mentioning that $\kappa_{\rm tot}$ is dependent on Q_i', which in turn depends on $\Delta\omega_{\rm pu}$.

Similar to Eq. (1), which phenomenologically describes slow saturation from a pump with ϕ, we also substitute $n_{\rm ph}^{0.5} \to n_{\rm ph}^{\phi}$ with $\phi < 0.5$ for all equations derived from the STM including Eqs. (4), (7), (8), and (11).

This is a second use of the low ϕ besides the MC model (which assumes a distribution of parameters, such as a distribution in p). However, we found that the MC model (see Appendix A) yielded a worse fit than Eq. (9), so it appears that only one group of p exists and it exhibits low power saturation. Assuming that the TLS distribution $dn \propto 1/\tau$, which is dependent on the coherence time τ [29] for a single value of p, we find that $\phi = 0.5$ (similar to Ref. [36]). As a result, we rule out the MC model and find that the FS model is qualitatively consistent.

From Eqs. (10) and (11), we extract $p = 1.5^{+0.8}_{-0.6}$ D $= 0.3^{+0.18}_{-0.1}$ eÅ, where consider isotropic angle distribution $\mathbf{p}$, $\langle|\mathbf{p}\cdot\hat{z}|\rangle = p/\sqrt{3}$ [53]. The precision of p is limited by the gap nonuniformity and more details can be found in Appendix B. For comparison, our two-tone spectroscopy is consistent with Andersson *et al.* [54], who resolved $\phi = 0.28$–0.3 in a surface acoustic wave resonator with the same method as we used to collect data in Fig. 2(d).

We show the temperature T dependence of the resonator loss $1/Q_i$ in Fig. 3(a). The loss is predominantly from MA interface TLSs, and at the lowest photon number the TLS loss is largest for the lowest temperatures. However, there is also loss seen at the high photon number $n_{\rm ph} = 10^4$ and $T = 250$ mK, where the photon number saturates the TLSs and the background loss remains, $1/Q_i^h = 1/Q_{i,0} - 1/Q_i(n_{\rm ph} = 10^4)$. Some of this loss is from temperature-induced quasiparticles in the aluminum wiring. To account for the high power loss, we fit these data using Eq. (5), and from C_1 found the $1/Q_i^h$ versus temperature in Fig. 3(b). It reveals large quasiparticle loss in two data points at $T \geq 200$ mK. The fit also gives the maximum and minimum jitter rates $\gamma_{\max}$ and $\gamma_{\min}$ of the LF TLS distribution, respectively, as shown in Fig. 3(c). The data show an increasing maximum jitter rate with increasing temperature and a minimum rate that is always larger than the Rabi frequency.

According to Ref. [55], CTLSs' decoherence rate $\Gamma_2 \propto T^{1+\mu}$ depends on the number of coupled LF TLSs. Here, μ describes a nonuniform TLS asymmetry energy Δ density: $P(\Delta) \propto \Delta^{\mu}$. This density-of-states dependence is

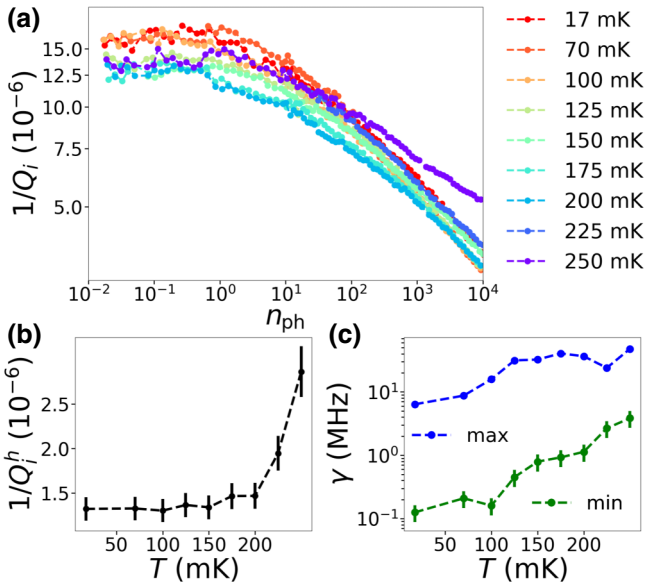

FIG. 3. (a) Plot of $1/Q_i$ versus $n_{\rm ph}$ in a SiN_x VGC resonator at different temperatures. The exponent of $Q_i^{-1}(n_{\rm ph})$ (ϕ) slightly decreases while the temperature increases. (b) The high-power background loss is defined as $1/Q_i^h = 1/Q_i(n_{\rm ph} = 10^4)$ for each temperature (see the text). This quantity is relatively constant for low temperature (< 200 mK) and increases at higher temperatures due to larger numbers of quasiparticles. (c) The extracted maximum and minimum jitter rates $\gamma_{\max,\,\min}$ increase with temperature. This is expected since γ is affected by the number of thermally activated low-frequency TLSs.

introduced phenomenologically and is stronger than the expected dipolar gap from TLS-TLS dipolar interactions [35]. Additionally, previous measurements [26,56] of $1/f$ resonant frequency noise induced by CTLSs show that the noise $\propto \Gamma_2^2/T = T^{1+2\mu}$ with $\mu \sim 0.3$. To study Γ_2 of MA TLSs, we perform a transmission S_{21} measurement on resonance at various temperatures and record the power spectral density (PSD) of the phase θ. Phase θ is defined as the angle between a vector defined from the off-resonant transmission [defined as $(1, 0)$] to the transmission $[S_{21}(t)]$ and the x axis [see the inset of Fig. 4(a)]. The PSD of the fluctuations in the phase angle, $\delta\theta$, provides information on the fluctuations in the resonator frequency [53]. The lower trace in panel (a) shows one data set of the PSD of $\delta\theta$. We fit this PSD to a function combining $1/f$, Lorentzian, and white noise: $S_{\delta\theta} = A/f^{\alpha} + B\tau/[1 + (2\pi f\,\tau)^2] + C$. The dominant low-frequency noise is considered $1/f$ type because the fit yielded $\alpha = 0.9$–1.1; this arises from many weakly coupled CTLSs [57,58]. The dashed guidelines show the Lorentzian noise and $1/f$ noise separately. In Fig. 4(b) we show the same data in the time domain ($\delta\theta$ versus time; blue) and the same data after a Gaussian filter in the time domain (red). The Lorentzian noise component in the fit yields $\tau \approx 3$ s, and as seen in Fig. 4(b), this yields telegraph-type resonant frequency switching (with a time

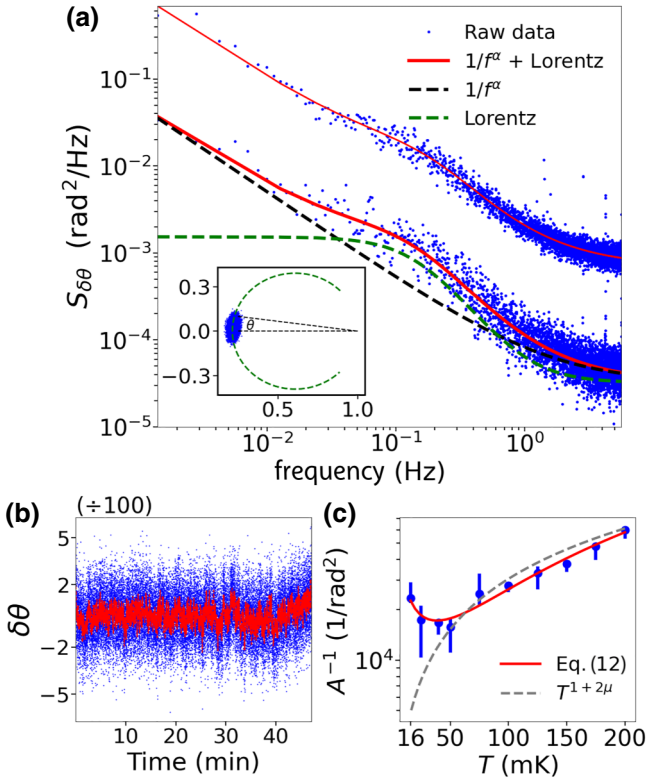

FIG. 4. Noise measurements from the SiN_x VG resonator and the probe n_{ph} is 1×10^{-2}. (a) Power spectral density (PSD) of the phase angle $\delta\theta = \theta - \bar{\theta}$, where θ is centered near zero in noise measurements. The inset shows the transmission data at one frequency on an I-Q plot of the resonance, where $\bar{\theta}$ is the mean value of θ in a dataset. PSD is fit (red curves) to a $1/f$ spectrum with Lorentz function and white noise $[A/f^{\alpha} + B\tau/(1 + (2\pi f\,\tau)^2) + C]$. An example trace and an average of eight separate measurements (shifted by 50 times) are shown on the bottom and top, respectively. (b) A plot of $\delta\theta$ versus time. The blue dots are the raw data, and we applied a Gaussian filter in time to obtain the set of smoothed red dots. (c) The inverse of A from the averaged PSD versus the temperature T. The error bar represents the max and min of A in eight separate measurements at each T. We assume that the TLS decoherence rate is temperature dependent, $\Gamma_2(T) = \Gamma_1/2 + \Gamma_\phi(T)$, where the LF-TLS-induced dephasing rate $\Gamma_\phi(T) \propto T^{1+\mu}$. From the red fit to Eq. (12), we obtain $\mu = 0.3 \pm 0.2$, which is consistent with the FS model (see the text).

much longer than $1/\gamma_{min}$). The cause of the switching is likely one strongly coupled CTLS that experiences low-frequency switching at a characteristic rate of 1/3 Hz. We find a smaller rate $1/\tau$ compared to our loss measurements and typical qubit measurements [57,59] due to the smaller sensitive bandwidths in this measurement.

The data of Fig. 4(b) show spectral diffusion (a drift in phase) in time. However, telegraph switching was not present in all data sets. Since $S_{\delta\theta}$ is a noise spectrum, it is logical that telegraph-type switching is sometimes hidden by $1/f$ noise, as observed. To show how the average value of Lorentzian noise may be smaller than in a single noise measurement, we average eight consecutive measurements in time and display the result in the upper trace in Fig. 4(a) (with a vertical shift; ×50 is on a log scale). From this procedure, the average $1/f$ noise amplitude (A) from the eight scans at different temperatures is obtained and plotted in Fig. 4(c), along with the minimum and maximum amplitudes from the eight scans that are shown as the limits of the vertical bars.

Current TLS noise theory gives $1/A \propto \Gamma_2^2/T$ and $\Gamma_2(T) \propto T^{1+\mu}$. From this formula for A we obtain $A = 1.7 \pm 0.2 \times 10^{-5}$ using our data at $T > 80$ mK [see the gray dashed line in Fig. 4(c)]. This magnitude is equivalent to $A = 1.4 \pm 0.2 \times 10^{-14}$ for the normalized noise $S_{\delta y} = S_{\delta\theta}/16Q^2$. Our value is within a factor of 2 of 2.4×10^{-14}, the value found in Ref. [26], and a few times larger than 3.5×10^{-15}, as found in Ref. [60].

Our fit value of μ is 0; however, the goodness of the fit to the standard function is poor. On the other hand, we find a better fit of $1/A$ to a similar phenomenological function,

$$\frac{1}{A} = \frac{(M + N\,T^{1+\mu})^2}{T}, \tag{12}$$

where the numerator is proportional to Γ_2^2, and M and N are constants. This equation can be understood by considering the fact that $\Gamma_2(T)$ has a T-independent term $\Gamma_{2,0}$ that gives $\Gamma_2(T) = \Gamma_{2,0} + \Gamma_\phi(T)$, and a mutual-TLS-induced dephasing rate remains as $\Gamma_\phi(T) \propto T^{1+\mu}$. The fit is shown as a red line and yields $\mu = 0.375 \pm 0.2$. Related to Eq. (12), Lucas *et al.* [61] found insufficient thermalization at the lowest temperatures and a flat background for A when T is below 80 mK. Another possible explanation is that the relaxation rate Γ_1 of our TLSs is higher than others such that $\Gamma_{2,0} = \Gamma_1/2$ is not ignorable. Since both explanations are possible in our devices, an additional measurement of surface-TLS coherence using a qubit may be necessary to ultimately understand this.

We also performed additional measurements of four measured SiN_x VGC resonators after an annealing process was added. This postannealing was performed under high vacuum at 300 °C for a duration of 1 h. After annealing, three of the four resonators were visible in spectroscopy, and the fourth likely had a collapsed capacitor. The gap distance is $d \approx 125$ nm and approximately constant in the majority of the devices, including those we report on in detail. We plot the two samples that showed the smallest and largest changes in distance. The postanneal distance is $d' \approx 125$ nm in sample A, which showed no change in distance, and sample B showed a change of 100 nm in distance. The quality factors of these resonators, before and after the anneal, are shown in Fig. 5. Prior to the anneal, the resonators show an approximately constant loss in different cooldowns as they age (see Appendix D). We show the results of two SiN_x VGCs, prior to and after annealing, and their fits to the FS model in Fig. 5. We

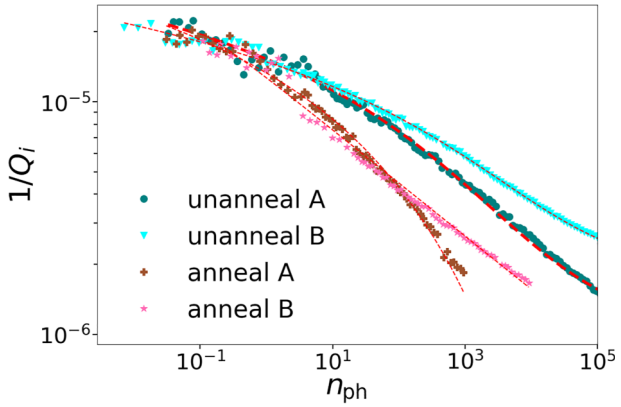

FIG. 5. Plot of $1/Q_i$ versus n_{ph} of unannealed and annealed SiN_x VGCs. The red dashed lines are the fits to Eq. (5). We observe that γ_{max} of the annealed VGCs are smaller than the unannealed VGCs. However, there is no improvement in the single photon Q_i^0. The probable cause of the decrease in γ_{max} and unchanged Q_i^0 is that the desorption of surface spins belongs to the set of LF TLSs, but not coherent TLSs.

find that the Q_i^0 and A are not changed significantly by annealing, in contrast to Ref. [26]. However, one obvious change is the slope of Q_i^0 versus n_{ph}. For postanneal A, γ_{max} and γ_{min} change from $2\pi \times (5.7\ \mathrm{MHz}, 20\ \mathrm{kHz})$ to $2\pi \times (1.9\ \mathrm{MHz}, 25\ \mathrm{kHz})$; for postanneal B, γ_{max} and γ_{min} change from $2\pi \times (2.5\ \mathrm{MHz}, 3.3\ \mathrm{kHz})$ to $2\pi \times (0.9\ \mathrm{MHz}, 11\ \mathrm{kHz})$. After annealing, we find that the number of photons needed for Q_i is reduced by 2 orders of magnitude. The improvement is likely caused by a reduction in the effective density of LF TLS due to the desorption of surface spins or rearrangement of surface atoms. It is also possible that the LF TLS density distribution as a function of γ is altered, but not captured in the theory [62].

V. DISCUSSION

The dimensionless parameter describing collective mutual TLS-TLS interaction, $\chi = P_{0,\mathrm{LF}} U_0 \approx 10^{-2}$–$10^{-3}$, is generally small in bulk materials and deposited films, which is critical for the steady-frequency approximation in the STM [35]. Here, $P_{0,\mathrm{LF}}$ is the LF TLS density and U_0 is the characteristic interaction factor of a (typical) TLS pair. In accordance with this, Q_i in our resonators containing deposited amorphous AlO_x films is proportional to $\sqrt{n_{\mathrm{ph}}}$ such that we expect that χ is small regardless of the observed TLS spectral diffusion in deposited films [27]. However, this study finds that the MA-TLS phenomena agree with the FS model. Thus, we expect that χ is larger on the Al surface than in deposited AlO_x films. The extracted p from the Al surface is $1.5^{+0.8}_{-0.6}$ D, which is only a few times smaller than p in a typical deposited amorphous film. In the standard theory, U_0 is expected to be similar in both samples if U_0 depends only on the electric dipole moment and the dielectric is thick enough that the typical bulk theory applies. Furthermore, from the postannealing experiment, we learn that $P_{0,\mathrm{LF}}$ is not necessarily equal to the density of CTLSs $P_{0,c}$, since $\tan\delta^0 \propto P_{0,c}$ is unchanged and γ_{max} is lowered via the annealing. Thus, two possible explanations for a larger χ of surface TLSs are that (1) the surface modifies the theory and (2) there is a much larger $P_{0,\mathrm{LF}}$ at the Al surface than in a deposited AlO_x film.

McRae *et al.* [63] reviewed the interface losses from a wide variety of materials, substrates, and processes through measurements of either lumped or coplanar waveguide resonators. The collective effect from different interfaces brings complexity and it is generally impossible to distinguish the effects from different interfaces. In the study of Refs. [14,47], the loss was extracted from different interfaces using different samples, but the power dependence of the loss of each interface was not extracted. Similar problems are found in the experiments of planar resonator frequency noise made from various superconductors [64].

VI. CONCLUSION

In the last decade, coplanar resonator studies have been important to the development of quantum information science. However, the loss of coplanar resonators limited by TLSs has a weak photon-number dependence $1/Q_i \propto n_{\mathrm{ph}}^{-\phi}$, where ϕ is a phenomenological fitting parameter that is measured at 0.18–0.22. This value is much smaller than the value 0.5 derived from the STM, which describes near-resonant TLSs as approximately steady in frequency. Coplanar resonators have multiple imperfect interfaces, which can host quantum defects. The STM can possibly explain this phenomenon as an MC model if multi-interfaces have different TLS types (dipole moment, relaxation rate) or possibly if a broad distribution of electric fields is included from the resonator geometry. In contrast, an FS TLS model, considering mutual interacting TLSs, yields a logarithmic power dependence [Eq. (5)]. Previous studies could not distinguish between these two models.

To understand the loss without multiple interface types or distributed fields, we studied resonators with VGCs. These allow us to probe MA-interface TLSs with an approximately uniform ac field due to approximately parallel metallic plates. We find that VGCs fabricated with a SiN_x sacrificial layer have an internal quality factor of $Q_i^0 \approxeq 20 \times 10^3$, which is consistent with AlOx loss. The weak n_{ph}-dependent loss is best fit to an FS model with one TLS type. This contrasts the loss properties of AlO_x films, which agree with the STM. In conclusion, using VGCs, we find that surface-based TLSs are distinguishable from bulk TLSs.

Next, we apply a two-tone spectroscopy and find that the maximum TLS Rabi frequency Ω_{max} is weakly dependent on the input power P_{in}. All of the equations used to analyze data are adjusted from the STM, such that we generalize

the power dependence as $n_{\rm pu}^{0.5} \rightarrow n_{\rm pu}^{\phi}$, including Eqs. (2), (7), (8), and (11). The last three equations were needed to analyze two-tone spectroscopy data, and all give $\phi \ll 0.5$. Therefore, we can exclude the MC model that predicts $\phi = 0.5$. Based on our data from a quasiparallel plate VGC, which gives a weak $n_{\rm ph}$ dependence to Q_i and $\Omega_{\rm max}$, we conclude that the TLSs are switching frequencies at a high rate and that the TLS dipoles have a p_z distribution width much smaller than its mean value.

We observe that the jitter rate of TLSs increases with temperature T from the measurement of the loss tangent. Additionally, we observe an increase in the TLS dephasing rate upon raising T from the resonant phase noise. These effects are qualitatively consistent with a model where noise from LF TLSs affect high-frequency (near resonant) TLSs [55]. Furthermore, we reduce the density of LF TLSs by postannealing in vacuum at 300 °C. As expected, this did not change the internal quality factor, which implies that low- and high-frequency TLSs have different sources.

Our study finds that surface TLSs, hosted in the MA interface on Al, are substantially different than TLSs hosted in deposited films. Specifically, TLSs in our vacuum-gap capacitors, in the analysis of power-dependent loss, two-tone saturation, and the frequency noise spectrum, exhibit more jitter than a standard deposited AlOx. This work is a significant step towards isolating and studying individual TLSs on a metal surface in a uniform ac electric field.

ACKNOWLEDGMENTS

We thank K. Cicak and R. Simmonds for scientific discussions on vacuum-gap capacitors.

APPENDIX A: ALTERNATIVE LOGARITHMIC EQUATION AND MULTICONTRIBUTION MODEL

In the main text we chose to fit using Eq. (5), which obeys the condition that $\gamma \gtrsim \Omega \gg \Gamma_1, \Gamma_2$ [36]. In this appendix, we first discuss two other possible models for fitting. The first equation derived in Ref. [36] is

$$\tan\delta_i = \tan\delta_i^0 P_\gamma \tanh\left(\frac{\hbar\omega_c}{2k_BT}\right)\ln\left(\frac{\gamma_{\rm max}\Gamma_2}{\Omega^2} + C_1\right), \quad \text{(A1)}$$

and is in a particular regime defined by $\gamma\Gamma_2 > \Omega^2$. A fit to Eq. (A1) is shown in Fig. 6(a), and we extract the geometric average $\sqrt{\gamma_{\rm max}\Gamma_2} = 2\pi \cdot 14$ MHz, which is much larger than Ω of the fitting range. However, since we do not know the value of Γ_2, we prefer Eq. (5) in the main text.

On the other hand, the MC model is given by Eq. (4) with $i = 1, \ldots, N$, while a more accurate integral form is shown in Eq. (3) and can also be found in Refs. [20,28]. Here, we consider the case of two contributions ($i = 1, 2$),

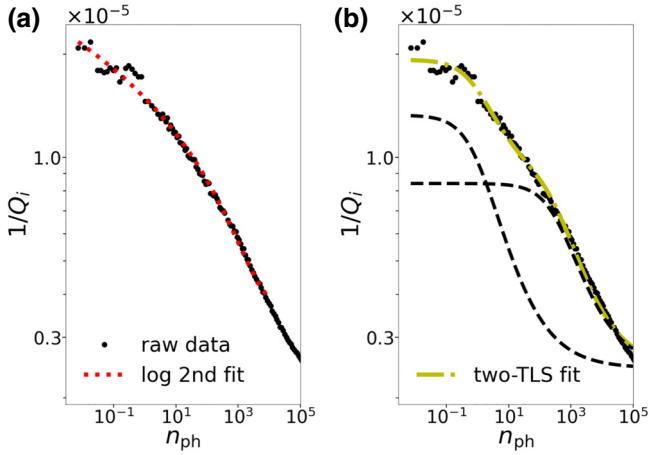

FIG. 6. Plot of $1/Q_i$ versus $n_{\rm ph}$ for two different fitting equations. (a) Fit to Eq. (A1) using $p = 1.5^{+0.8}_{-0.6}$ D, as given in Fig. 2(d). The fit yields the geometric average $\sqrt{\gamma_{\rm max}\Gamma_2} = 2\pi \cdot$ 14MHz. (b) Fit to Eq. (A2). We obtain the fitting parameters $F_1 \tan\delta_1^0 = 1.1 \times 10^{-5}$, $F_2 \tan\delta_2^0 = 6.0 \times 10^{-6}$, $n_{c,1} = 0.9$, and $n_{c,2} = 320$. The two dashed guidelines represent the contributions from each TLS contribution. However, from Fig. 2(d), we exclude the possibility that Eq. (A2) is the correct equation (see the main text).

giving

$$\tan\delta(n_{\rm ph}) = \frac{F_1 \tan\delta_1^0}{\sqrt{1 + n_{\rm ph}/n_{c,1}}} + \frac{F_2 \tan\delta_2^0}{\sqrt{1 + n_{\rm ph}/n_{c,2}}} + C_0. \quad \text{(A2)}$$

From the fit in Fig. 6(b), we obtain $F_1 \tan\delta_1^0 = 1.1 \times 10^{-5}$, $F_2 \tan\delta_2^0 = 6.0 \times 10^{-6}$, $n_{c,1} = 0.9$, and $n_{c,2} = 320$. Two guidelines show two separate square-root dependent Q_i. According to the STM [4,5], $n_{c,i}^{-1} \propto (p_i E_{\rm zp})^2 \tau$, where p_i is the dipole moment of the ith group. The fit yields $n_{c,2}/n_{c,1} \approx 320$, which is valid only if there are two types of TLSs.

However, the validity is negated by the results of the two-tone spectroscopy measurement. In Fig. 7, we observe that Eq. (11) (red) is a better fitting function than Eq. (9) (blue) for the raw data in black when $\Delta\omega_{\rm pu}$ is far detuned. Even assuming two TLS groups with $p_1 = \sqrt{320}p_2$, as shown in green, $\Delta\omega$ does not match the raw data. More details of the two-tone technique are found in the main text.

APPENDIX B: UNCERTAINTY IN THE DIPOLE MOMENTS

The accuracies of d and $n_{\rm pu}$ heavily affect the extracted value of p. To obtain the average d, we compared measured frequencies to simulated frequencies, where the latter is obtained on the resonator structure simulated in COMSOL with a meander inductor and uniform gap capacitor. The kinetic inductance in our Al meander is not included in

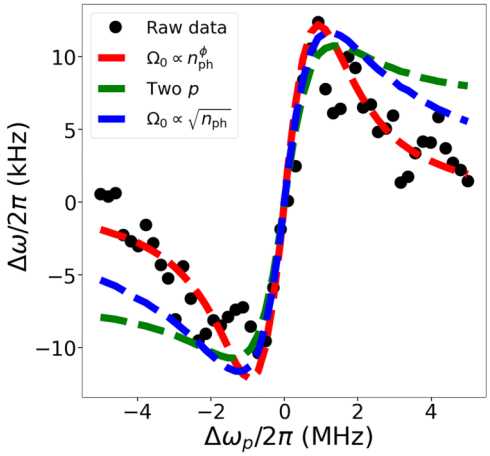

FIG. 7. Two-tone spectroscopy, $\Delta\omega$ versus $\Delta\omega_{\rm pu}$, using different models to fit. The black dots and the red curve are the same as in Fig. 2(b). The blue and green curves are based on the STM with one and two groups of TLSs, respectively. We find that only a weak power dependence Ω_0 can explain the behavior of $\Delta\omega$ while increasing $\Delta\omega_{\rm pu}$.

the simulation, but the film thickness (100 nm) is much larger than the penetration depth such that the geometric inductance dominates.

Recall that the gap in the capacitor is not precisely uniform and also that the cooldown is known to bend the capacitor. However, we know the gap at the supports and also the resonator frequency related to the gap distribution. Using these constraints, we simulate the capacitor using a COMSOL simulation and find an average gap distance of $d = 125$ nm. Figure 8 shows the simulation of the electric field distribution using the bending downward structure in Fig. 1(b). We assumed that the bending of the top bridge followed a quadratic equation symmetrically, related to the supporting posts, where the height is precisely fabricated. The simulation with correction for the same capacitance as the uniform model

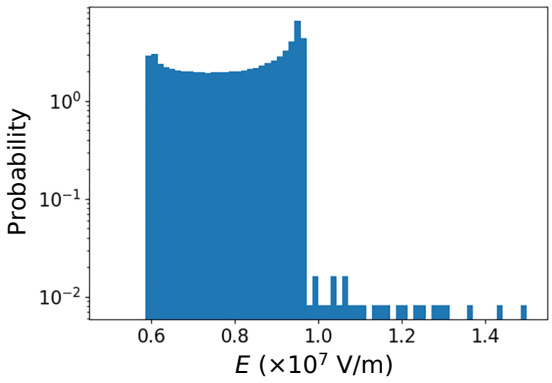

FIG. 8. The electric field distribution is simulated using COMSOL with one voltage on one side. The standard deviation of the electric field is 16% of the mean value.

gives a center height of 0.104 μm and a quadratic coefficient of 8.4×10^{-3} ($\mu{\rm m}^{-1}$). The calculated gap distribution has a standard deviation of $\Delta d = 16\%$ from the mean value.

In our measurement of the device, the limit to precision is caused by the nonuniform gap distance d. However, we also used the standard practice of calibrating our input power using room-temperature data. This results in some systematic inaccuracy to p that we have not carefully characterized. It is possible that our inaccuracy from the input power calibration is larger than the uncertainty caused by capacitor gap nonuniformity.

APPENDIX C: VOLTAGE-TUNABLE RESONANCE AND NONLINEAR OSCILLATOR

We are able to apply a voltage bias V_b on the capacitors in our design. The accumulated charges on the electrodes

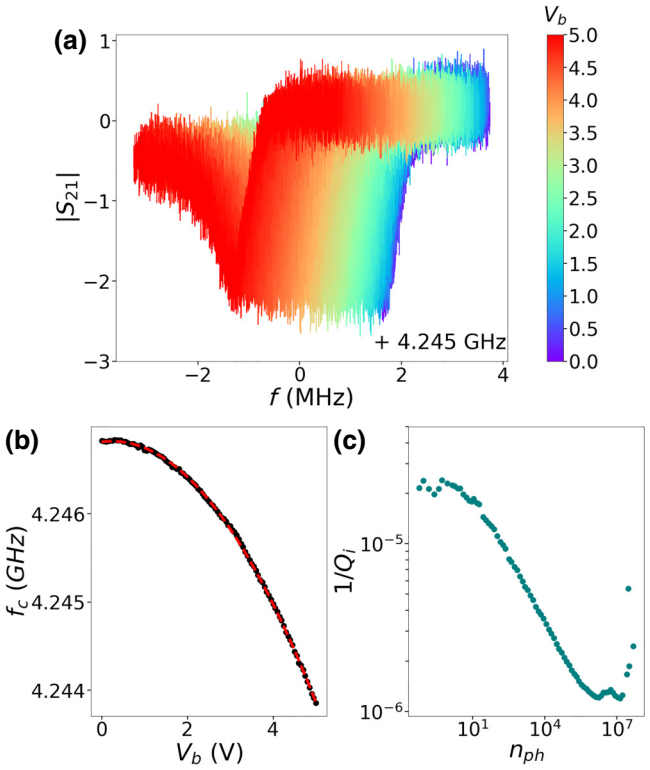

FIG. 9. Resonance shift due to voltage biasing. (a) The magnitude of transmission $|S_{21}|$ at different voltage biases V_b. Different colors show the range of V_b values, from $V_b = 0$ V (purple) to $V_b = 5$ V (red). (b) Resonance f_c versus V_b. We found a quadratic decrease in f_c and the fit to $m_2 V_b^2 + m_1 V_b + m_0$, shown with the red line, where $m_2 = -0.13$ (MHz/V^2), $m_1 = 0.06$ (MHz/V), and $m_0 = 4.2468$ (GHz). (c) Plot of $1/Q_i$ versus $n_{\rm ph}$ from a SiN_x VGC. When $n_{\rm ph} > 5 \times 10^6$, $\tan\delta(n_{\rm ph})$ increases due to the high-power-induced quasiparticles. The maximum ac voltage amplitude across the capacitor is $\sqrt{2hf_c n_{\rm ph}/C} = 12$ mV, which does not cause an obvious frequency shift or extra complexity, corresponding to $n_{\rm ph} = 5 \times 10^6$.

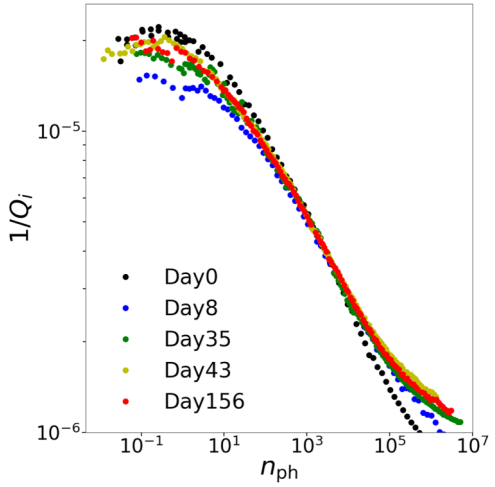

FIG. 10. The aging effect on a SiN_x VGC. "Day0" indicates the resonator is in the vacuum immediately after the releasing process. We find that the jitter rate γ_{max} is slightly increased with time, but that the changes are small.

would attract and bring two electrodes closer, resulting in a decrease in the resonance frequency. In Figs. 9(a) and 9(b), we show the magnitude of transmission S_{21} and the resonance f_c at various V_b. The $f_c(V_b)$ shows a quadratic dependence: $m_2 V_b^2 + m_1 V_b + m_0$ with $m_2 = -0.13$ (MHz/V^2), $m_1 = 0.06$ (MHz/V), and $m_0 = 4.2468$ (GHz). The red fit line is shown in Fig. 9(b). In Fig. 9(c), the resonator has nonlinearity when the stored photon number $n_{\mathrm{ph}} > 5 \times 10^6$. The amplitude of the voltage $\delta V = \sqrt{2hf_c n_{\mathrm{ph}}/C} = 12$ mV when $n_{\mathrm{ph}} = 5 \times 10^6$. Since this amplitude is too small to attract the plates, we conclude that the extra loss is due to the quasiparticles created by Cooper pairs broken by up-converted photons.

APPENDIX D: VGC AGING EFFECT

We found a small aging effect in our SiN_x VGC. In Fig. 10, we show $1/Q_i$ for one SiN_x VGC from immediately after the VGC was released on day 0 (about 2 h to be pumped into vacuum) to day N (where N is the number of days after releasing and of exposure of the MA interface to ambient conditions). A slightly increased γ_{max} was found over time that implies some accumulation of LF TLSs.

[1] J. M. Martinis, K. B. Cooper, R. McDermott, M. Steffen, M. Ansmann, K. D. Osborn, K. Cicak, S. Oh, D. P. Pappas, R. W. Simmonds, and C. C. Yu, Decoherence in Josephson qubits from dielectric loss, Phys. Rev. Lett. **95**, 210503 (2005).

[2] J. M. Gambetta, J. M. Chow, and M. Steffen, Building logical qubits in a superconducting quantum computing system, Npj Quantum Inf. **3**, 1 (2017).

[3] E. J. Connors, J. Nelson, H. Qiao, L. F. Edge, and J. M. Nichol, Low-frequency charge noise in Si/SiGe quantum dots, Phys. Rev. B **100**, 165305 (2019).

[4] P. W. Anderson, B. Halperin, and C. M. Varma, Anomalous low-temperature thermal properties of glasses and spin glasses, Philos. Mag. **25**, 1 (1972).

[5] W. Phillips, Tunneling states in amorphous solids, J. Low Temp. Phys. **7**, 351 (1972).

[6] H. Paik and K. D. Osborn, Reducing quantum-regime dielectric loss of silicon nitride for superconducting quantum circuits, Appl. Phys. Lett. **96**, 072505 (2010).

[7] J. Suh, A. Weinstein, and K. Schwab, Optomechanical effects of two-level systems in a back-action evading measurement of micro-mechanical motion, Appl. Phys. Lett. **103**, 052604 (2013).

[8] J. Gao, M. Vissers, M. Sandberg, F. Da Silva, S. W. Nam, D. Pappas, D. Wisbey, E. Langman, S. Meeker, B. Mazin *et al.*, A titanium-nitride near-infrared kinetic inductance photon-counting detector and its anomalous electrodynamics, Appl. Phys. Lett. **101**, 142602 (2012).

[9] T. White, J. Mutus, I.-C. Hoi, R. Barends, B. Campbell, Y. Chen, Z. Chen, B. Chiaro, A. Dunsworth, E. Jeffrey *et al.*, Traveling wave parametric amplifier with Josephson junctions using minimal resonator phase matching, Appl. Phys. Lett. **106**, 242601 (2015).

[10] T. Ramos, V. Sudhir, K. Stannigel, P. Zoller, and T. J. Kippenberg, Nonlinear quantum optomechanics via individual intrinsic two-level defects, Phys. Rev. Lett. **110**, 193602 (2013).

[11] J. M. Fink, M. Kalaee, A. Pitanti, R. Norte, L. Heinzle, M. Davanço, K. Srinivasan, and O. Painter, Quantum electromechanics on silicon nitride nanomembranes, Nat. Commun. **7**, 1 (2016).

[12] C. Wang, C. Axline, Y. Y. Gao, T. Brecht, Y. Chu, L. Frunzio, M. Devoret, and R. J. Schoelkopf, Surface participation and dielectric loss in superconducting qubits, Appl. Phys. Lett. **107**, 162601 (2015).

[13] J. M. Gambetta, C. E. Murray, Y.-K.-K. Fung, D. T. McClure, O. Dial, W. Shanks, J. W. Sleight, and M. Steffen, Investigating surface loss effects in superconducting transmon qubits, IEEE Trans. Appl. Supercond. **27**, 1 (2016).

[14] W. Woods, G. Calusine, A. Melville, A. Sevi, E. Golden, D. K. Kim, D. Rosenberg, J. L. Yoder, and W. D. Oliver, Determining interface dielectric losses in superconducting coplanar-waveguide resonators, Phys. Rev. Appl. **12**, 014012 (2019).

[15] J. Verjauw, A. Potočnik, M. Mongillo, R. Acharya, F. Mohiyaddin, G. Simion, A. Pacco, T. Ivanov, D. Wan, A. Vanleenhove *et al.*, Investigation of microwave loss induced by oxide regrowth in high-Q niobium resonators, Phys. Rev. Appl. **16**, 014018 (2021).

[16] M. Mergenthaler, S. Paredes, P. Müller, C. Müller, S. Filipp, M. Sandberg, J. Hertzberg, V. Adiga, M. Brink, and A. Fuhrer, Ultrahigh vacuum packaging and surface cleaning for quantum devices, Rev. Sci. Instrum. **92**, 025121 (2021).

[17] A. Megrant, C. Neill, R. Barends, B. Chiaro, Y. Chen, L. Feigl, J. Kelly, E. Lucero, M. Mariantoni, P. J. O'Malley *et al.*, Planar superconducting resonators with internal quality factors above one million, Appl. Phys. Lett. **100**, 113510 (2012).

[18] T. Lindström, J. Healey, M. Colclough, C. Muirhead, and A. Y. Tzalenchuk, Properties of superconducting planar resonators at millikelvin temperatures, Phys. Rev. B **80**, 132501 (2009).

[19] D. P. Pappas, M. R. Vissers, D. S. Wisbey, J. S. Kline, and J. Gao, Two level system loss in superconducting microwave resonators, IEEE Trans. Appl. Supercond. **21**, 871 (2011).

[20] M. Khalil, M. Stoutimore, S. Gladchenko, A. Holder, C. Musgrave, A. Kozen, G. Rubloff, Y. Liu, R. Gordon, J. Yum *et al.*, Evidence for hydrogen two-level systems in atomic layer deposition oxides, Appl. Phys. Lett. **103**, 162601 (2013).

[21] S. T. Skacel, C. Kaiser, S. Wuensch, H. Rotzinger, A. Lukashenko, M. Jerger, G. Weiss, M. Siegel, and A. V. Ustinov, Probing the density of states of two-level tunneling systems in silicon oxide films using superconducting lumped element resonators, Appl. Phys. Lett. **106**, 022603 (2015).

[22] M. S. Khalil, F. Wellstood, and K. D. Osborn, Loss dependence on geometry and applied power in superconducting coplanar resonators, IEEE Trans. Appl. Supercond. **21**, 879 (2010).

[23] P. Macha, S. van Der Ploeg, G. Oelsner, E. Il'ichev, H.-G. Meyer, S. Wünsch, and M. Siegel, Losses in coplanar waveguide resonators at millikelvin temperatures, Appl. Phys. Lett. **96**, 062503 (2010).

[24] C. Müller, J. H. Cole, and J. Lisenfeld, Towards understanding two-level-systems in amorphous solids: Insights from quantum circuits, Rep. Prog. Phys. **82**, 124501 (2019).

[25] J. Burnett, L. Faoro, I. Wisby, V. Gurtovoi, A. Chernykh, G. Mikhailov, V. Tulin, R. Shaikhaidarov, V. Antonov, P. Meeson *et al.*, Evidence for interacting two-level systems from the $1/f$ noise of a superconducting resonator, Nat. Commun. **5**, 1 (2014).

[26] S. De Graaf, L. Faoro, J. Burnett, A. Adamyan, A. Y. Tzalenchuk, S. Kubatkin, T. Lindström, and A. Danilov, Suppression of low-frequency charge noise in superconducting resonators by surface spin desorption, Nat. Commun. **9**, 1 (2018).

[27] C.-C. Hung, L. Yu, N. Foroozani, S. Fritz, D. Gerthsen, and K. D. Osborn, Probing hundreds of individual quantum defects in polycrystalline and amorphous alumina, Phys. Rev. Appl. **17**, 034025 (2022).

[28] N. Gorgichuk, T. Junginger, and R. de Sousa, Origin of dielectric loss at the Nb/oxide interface: Evidence for atomic two-level systems, arXiv:2203.05054.

[29] T. Palomaki, S. Dutta, R. Lewis, A. Przybysz, H. Paik, B. Cooper, H. Kwon, J. Anderson, C. Lobb, F. Wellstood *et al.*, Multilevel spectroscopy of two-level systems coupled to a dc SQUID phase qubit, Phys. Rev. B **81**, 144503 (2010).

[30] B. Sarabi, A. N. Ramanayaka, A. L. Burin, F. C. Wellstood, and K. D. Osborn, Projected dipole moments of individual two-level defects extracted using circuit quantum electrodynamics, Phys. Rev. Lett. **116**, 167002 (2016).

[31] L. Yu, S. Matityahu, Y. J. Rosen, C.-C. Hung, A. Maksymov, A. L. Burin, M. Schechter, and K. D. Osborn, Evidence for weakly and strongly interacting two-level systems in amorphous silicon, arXiv:2110.10747.

[32] P. Klimov, J. Kelly, Z. Chen, M. Neeley, A. Megrant, B. Burkett, R. Barends, K. Arya, B. Chiaro, Y. Chen *et al.*, Fluctuations of energy-relaxation times in superconducting qubits, Phys. Rev. Lett. **121**, 090502 (2018).

[33] J. Lisenfeld, G. J. Grabovskij, C. Müller, J. H. Cole, G. Weiss, and A. V. Ustinov, Observation of directly interacting coherent two-level systems in an amorphous material, Nat. Commun. **6**, 1 (2015).

[34] C. Yu and A. Leggett, Low temperature properties of amorphous materials: through a glass darkly, Comments Cond. Mat. Phys **14**, 231 (1988).

[35] A. L. Burin, D. Natelson, D. D. Osheroff, and Y. Kagan, in *Tunneling Systems in Amorphous and Crystalline Solids* (Springer Berlin Heidelberg, Berlin, Heidelberg, 1998), pp. 223–315.

[36] L. Faoro and L. B. Ioffe, Internal loss of superconducting resonators induced by interacting two-level systems, Phys. Rev. Lett. **109**, 157005 (2012).

[37] T. Capelle, E. Flurin, E. Ivanov, J. Palomo, M. Rosticher, S. Chua, T. Briant, P.-F. Cohadon, A. Heidmann, T. Jacqmin *et al.*, Probing a two-level system bath via the frequency shift of an off-resonantly driven cavity, Phys. Rev. Appl. **13**, 034022 (2020).

[38] N. Kirsh, E. Svetitsky, A. L. Burin, M. Schechter, and N. Katz, Revealing the nonlinear response of a tunneling two-level system ensemble using coupled modes, Phys. Rev. Materials **1**, 012601 (2017).

[39] J. D. Brehm, A. Bilmes, G. Weiss, A. V. Ustinov, and J. Lisenfeld, Transmission-line resonators for the study of individual two-level tunneling systems, Appl. Phys. Lett. **111**, 112601 (2017).

[40] M. Khalil, S. Gladchenko, M. Stoutimore, F. Wellstood, A. Burin, and K. Osborn, Landau-Zener population control and dipole measurement of a two-level-system bath, Phys. Rev. B **90**, 100201 (2014).

[41] A. L. Burin, M. S. Khalil, and K. D. Osborn, Universal dielectric loss in glass from simultaneous bias and microwave fields, Phys. Rev. Lett. **110**, 157002 (2013).

[42] S. de Graaf, L. Faoro, L. Ioffe, S. Mahashabde, J. Burnett, T. Lindström, S. Kubatkin, A. Danilov, and A. Y. Tzalenchuk, Two-level systems in superconducting quantum devices due to trapped quasiparticles, Sci. Adv. **6**, eabc5055 (2020).

[43] C. Deng, M. Otto, and A. Lupascu, Characterization of low-temperature microwave loss of thin aluminum oxide formed by plasma oxidation, Appl. Phys. Lett. **104**, 043506 (2014).

[44] H. Mamin, E. Huang, S. Carnevale, C. Rettner, N. Arellano, M. Sherwood, C. Kurter, B. Trimm, M. Sandberg, R. Shelby *et al.*, Merged-element transmons: Design and qubit performance, Phys. Rev. Appl. **16**, 024023 (2021).

[45] A. Bilmes, S. Volosheniuk, J. D. Brehm, A. V. Ustinov, and J. Lisenfeld, Quantum sensors for microscopic tunneling systems, Npj Quantum Inf. **7**, 1 (2021).

[46] A. Bilmes, A. Megrant, P. Klimov, G. Weiss, J. M. Martinis, A. V. Ustinov, and J. Lisenfeld, Resolving the positions of defects in superconducting quantum bits, Sci. Rep. **10**, 1 (2020).

[47] A. Melville, G. Calusine, W. Woods, K. Serniak, E. Golden, B. M. Niedzielski, D. K. Kim, A. Sevi, J. L. Yoder, E.

A. Dauler *et al.*, Comparison of dielectric loss in titanium nitride and aluminum superconducting resonators, Appl. Phys. Lett. **117**, 124004 (2020).

[48] J. Burnett, L. Faoro, and T. Lindström, Analysis of high quality superconducting resonators: Consequences for TLS properties in amorphous oxides, Supercond. Sci. Technol. **29**, 044008 (2016).

[49] K. Cicak, D. Li, J. A. Strong, M. S. Allman, F. Altomare, A. J. Sirois, J. D. Whittaker, J. D. Teufel, and R. W. Simmonds, Low-loss superconducting resonant circuits using vacuum-gap-based microwave components, Appl. Phys. Lett. **96**, 093502 (2010).

[50] J. D. Teufel, D. Li, M. Allman, K. Cicak, A. Sirois, J. Whittaker, and R. Simmonds, Circuit cavity electromechanics in the strong-coupling regime, Nature **471**, 204 (2011).

[51] T. Palomaki, J. Teufel, R. Simmonds, and K. W. Lehnert, Entangling mechanical motion with microwave fields, Science **342**, 710 (2013).

[52] S. M. Girvin, in *Quantum Machines: Measurement and Control of Engineered Quantum Systems* (Oxford University Press Oxford, 2014), Vol. 96, pp. 113–256.

[53] J. Gao, Ph.D. thesis, California Institute of Technology, 2008.

[54] G. Andersson, A. L. O. Bilobran, M. Scigliuzzo, M. M. de Lima, J. H. Cole, and P. Delsing, Acoustic spectral hole-burning in a two-level system ensemble, Npj Quantum Inf. **7**, 1 (2021).

[55] L. Faoro and L. B. Ioffe, Interacting tunneling model for two-level systems in amorphous materials and its predictions for their dephasing and noise in superconducting microresonators, Phys. Rev. B **91**, 014201 (2015).

[56] A. Ramanayaka, B. Sarabi, and K. Osborn, Evidence for universal relationship between the measured $1/f$ permittivity noise and loss tangent created by tunneling atoms, arXiv:1507.06043.

[57] J. J. Burnett, A. Bengtsson, M. Scigliuzzo, D. Niepce, M. Kudra, P. Delsing, and J. Bylander, Decoherence benchmarking of superconducting qubits, Npj Quantum Inf. **5**, 1 (2019).

[58] D. Niepce, J. J. Burnett, M. Kudra, J. H. Cole, and J. Bylander, Stability of superconducting resonators: Motional narrowing and the role of Landau-Zener driving of two-level defects, Sci. Adv. **7**, eabh0462 (2021).

[59] S. Schlör, J. Lisenfeld, C. Müller, A. Bilmes, A. Schneider, D. P. Pappas, A. V. Ustinov, and M. Weides, Correlating decoherence in transmon qubits: Low frequency noise by single fluctuators, Phys. Rev. Lett. **123**, 190502 (2019).

[60] J. Burnett, A. Bengtsson, D. Niepce, and J. Bylander, Noise and loss of superconducting aluminium resonators at single photon energies, J. Phys.: Conf. Ser. **969**, 012131 (2018).

[61] M. Lucas, A. Danilov, L. Levitin, A. Jayaraman, A. Casey, L. Faoro, A. Y. Tzalenchuk, S. Kubatkin, J. Saunders, and S. de Graaf, Quantum bath suppression in a superconducting circuit by immersion cooling, arXiv:2210.03816.

[62] *private conversation with Burin, Alexander*.

[63] C. R. H. McRae, H. Wang, J. Gao, M. R. Vissers, T. Brecht, A. Dunsworth, D. P. Pappas, and J. Mutus, Materials loss measurements using superconducting microwave resonators, Rev. Sci. Instrum. **91**, 091101 (2020).

[64] R. Barends, H. Hortensius, T. Zijlstra, J. J. Baselmans, S. Yates, J. Gao, and T. M. Klapwijk, Noise in NbTiN, Al, and Ta superconducting resonators on silicon and sapphire substrates, IEEE Trans. Appl. Supercond. **19**, 936 (2009).